

Available online at [www.sciencedirect.com](http://www.sciencedirect.com)

SCIENCE @ DIRECT®

EPSL

Earth and Planetary Science Letters xx (2006) xxx–xxx

[www.elsevier.com/locate/epsl](http://www.elsevier.com/locate/epsl)

# Grain size sensitive deformation mechanisms in naturally deformed peridotites

Jessica M. Warren <sup>a,\*</sup>, Greg Hirth <sup>b</sup>

<sup>a</sup> MIT/WHOI Joint Program, Woods Hole, MA 02540, USA

<sup>b</sup> Woods Hole Oceanographic Institution, Woods Hole, MA 02540, USA

Received 6 April 2005; received in revised form 5 June 2006; accepted 6 June 2006

Editor: R.D. van der Hilst

## Abstract

Microstructural analyses of peridotite mylonites from the oceanic lithosphere indicate that shear localization results from the combined effects of grain size reduction, grain boundary sliding and second phase pinning during deformation. The pinning effect, combined with experimental flow laws for olivine, suggests that a permanent transition from dislocation creep processes to diffusion creep occurs. This rheological transition provides a mechanism for long term weakening of the lithosphere for rocks deforming in the brittle–ductile regime. In addition, our results support the hypothesis that a transition to diffusion creep promotes the randomization of pre-existing lattice preferred orientations, which would reduce seismic anisotropy.

© 2006 Elsevier B.V. All rights reserved.

*Keywords:* mylonites; olivine; grain boundary sliding; lattice preferred orientation; anisotropy

## 1. Introduction

The observation of fine grained mylonites in shear zones indicates that grain size sensitive creep processes promote strain localization (e.g., [1–7]). For the sample in Fig. 1, microstructural observations show that ductile deformation resulted in three orders of magnitude grain size reduction. Peridotite mylonites are commonly sampled from oceanic fracture zones [4]. The geologic provenance of these mylonites suggests that they formed in the ductile region of the lithosphere along the down-dip extension of transform faults. We describe fabrics in a peridotite mylonite from the Shaka Fracture Zone that

support extrapolation of experimentally determined rheological data [8] to geologic conditions appropriate for the oceanic lithosphere. We conclude that grain boundary sliding and grain boundary pinning lead to permanent grain size reduction and strain localization.

Previous studies of peridotite mylonites in orogenic massifs and ophiolites have interpreted grain size reduction in mylonites as the result of (i) fluid addition (e.g., [9]), (ii) reaction with melt (e.g., [10]), and (iii) the breakdown reaction of spinel to plagioclase with decreasing pressure (e.g., [11,6]); see [3] for a review of earlier literature. Vissers et al. [9] interpreted the microstructures in Erro Tobbio lherzolite mylonites as resulting from a wet olivine rheology with reaction-related grain size reduction. Dijkstra et al. [10] concluded that a melt-present reaction promoted grain size sensitive deformation in shear zone mylonites from

\* Corresponding author. Tel.: +1 508 289 3749.

E-mail addresses: [jmwarren@whoi.edu](mailto:jmwarren@whoi.edu) (J.M. Warren), [ghirth@whoi.edu](mailto:ghirth@whoi.edu) (G. Hirth).

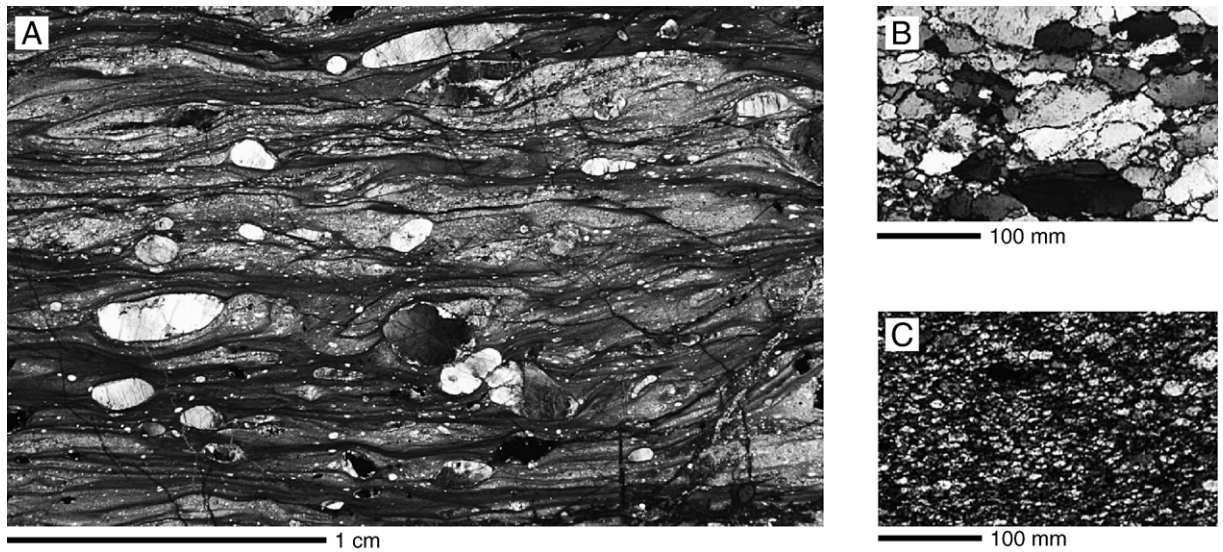


Fig. 1. (A) Photomicrograph of ultra-mylonite peridotite sample AII-107-61-83 from the Shaka Fracture Zone on the Southwest Indian Ridge. Grain size sensitive deformation has resulted in the formation of anastomosing bands of coarser ( $<100\ \mu\text{m}$ ) and finer ( $<10\ \mu\text{m}$ ) grained olivine, with distributed grains of orthopyroxene, clinopyroxene and spinel. Large porphyroclasts of olivine, orthopyroxene, clinopyroxene, spinel and coarser grained olivine aggregates remain and appear to have behaved as hard inclusions during deformation. (B) Photomicrograph of a coarser grained area of the ultra-mylonite, with a grain size range of  $1\text{--}100\ \mu\text{m}$ . (C) Photomicrograph of a finer grained area, with an olivine grain size of  $1\text{--}10\ \mu\text{m}$ .

the Othris peridotite massif. In the Turon de Técoüere peridotite shear zone, Newman et al. [6] suggested that grain size reduction resulted from the spinel to plagioclase phase transition reaction.

Several lines of evidence indicate that the Shaka Fracture Zone mylonites deformed in the absence of water and melt, and that breakdown reactions were not involved. We find no syn-deformational hydrous phases such as amphibole, talc or serpentine. The mantle at fracture zones is expected to be dehydrated and depleted due to earlier on-axis melting and melt extraction [12]. In addition to the lack of evidence for melt or water involvement in the mylonite deformation, we find no indication of reaction enhancement via the breakdown of spinel to plagioclase. The rare earth element concentrations measured by ion microprobe in a clinopyroxene porphyroclast have the typical depleted compositions found in other abyssal peridotites [13], with no Eu anomaly, which is a sensitive indicator of plagioclase formation [14].

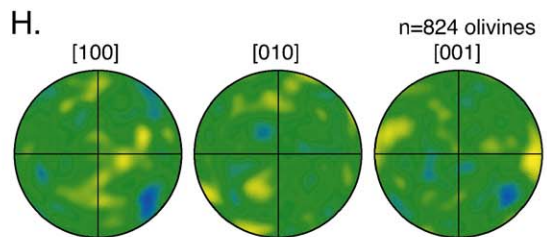
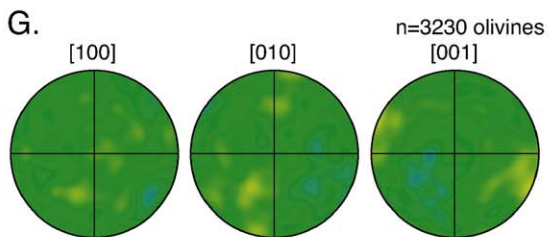
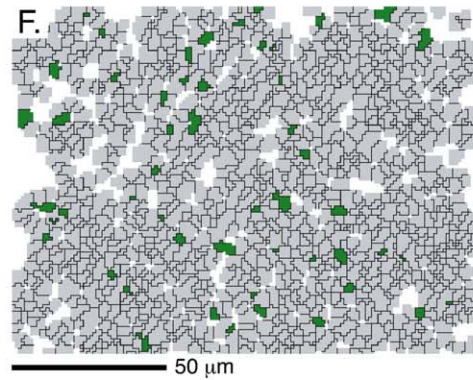
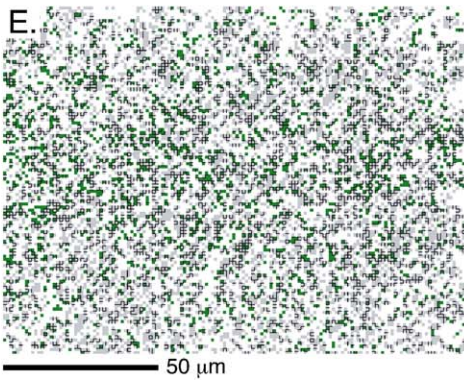
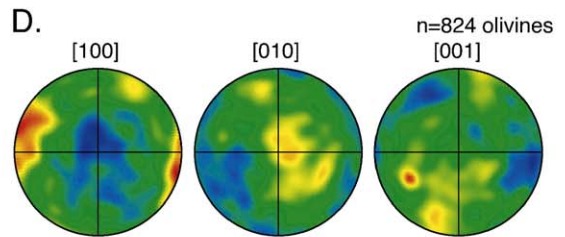
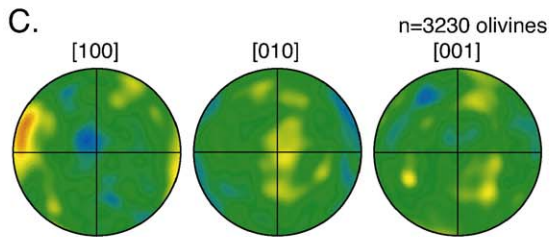
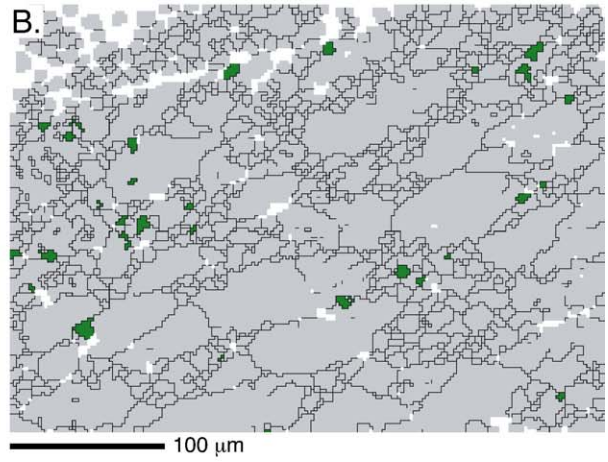
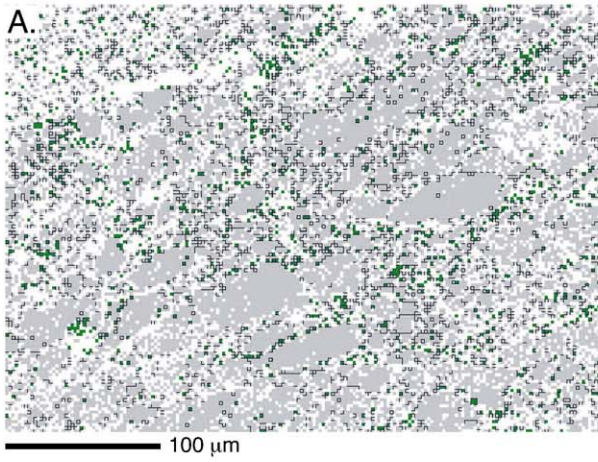
## 2. Methods

To study deformation mechanisms in mylonites, we used electron backscatter diffraction (EBSD) to analyze olivine and orthopyroxene crystal orientations in thin sections of mylonitized peridotites cut parallel to lineation and perpendicular to foliation. We made orientation measurements down to a  $1\ \mu\text{m}$  grain size,

an order of magnitude smaller size than that accessible with a U-stage. In addition, EBSD permits identification and quantification of the distribution of secondary phases. Data were gathered using an electron backscatter detector attached to a JEOL 840 SEM. Portions of thin sections were mapped for lattice orientation in 1, 2, or 4  $\mu\text{m}$  steps (depending on the average grain size of the region being mapped), using a rasterized beam across the sample surface. EBSD patterns were processed and analyzed using HKL Technology's Channel 5 software package.

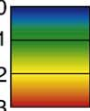
Orientation maps in Figs. 2–4 contain from 52% to 72% indexed data. Non-indexed (white) pixels represent points with a mean angular deviation (MAD) number  $\geq 1^\circ$ , which result from surface roughness and computer mis-indexing. The MAD number quantifies the mismatch between lattice planes in the calculated orientation and those quantified from the digitized bands of the diffraction pattern. Raw data, consisting of all indexed points with a MAD number  $< 1^\circ$ , are shown as maps and pole figures for coarser and finer grained regions in Fig. 2. Processed data, for which wild spikes have been removed and all pixels with zero solutions have been extrapolated, are also shown in Fig. 2. Wild spikes are single pixels (i) which are misoriented by  $> 10^\circ$  from the average orientation of the surrounding eight pixels and (ii) for which the maximum misorientation between any two of the surrounding pixels is  $< 10^\circ$ . All pixels which are wild spikes or have a MAD number  $> 1^\circ$  are replaced





Shear plane  


Pole Figures: 0  
 Contoured as  
 multiples of a  
 uniform distribution  
 3



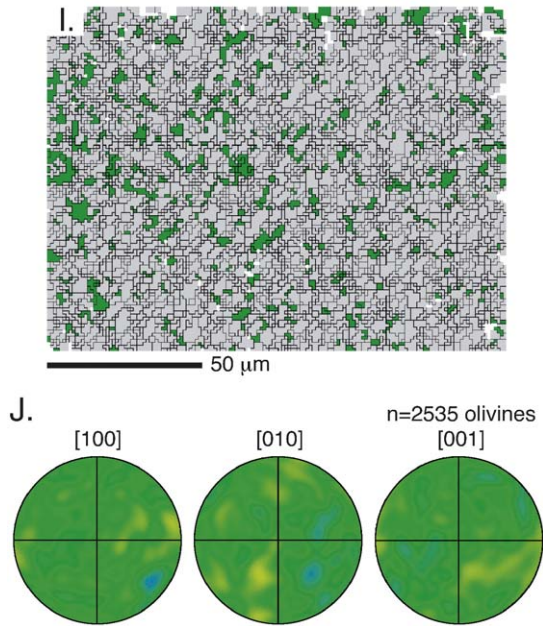


Fig. 2. Maps of raw data collected in a coarser grained area (A) and a finer grained area (E) of the ultra-mylonite. The coarser grained area was collected at a 2  $\mu\text{m}$  step size with a total of 64% of the area indexed; the finer grained area was collected at a 1  $\mu\text{m}$  step size with 52% indexed. Each grey point represents an olivine orientation collected by EBSD and green points represent secondary phases (orthopyroxene, clinopyroxene, and spinel) for which orientations were measured. White points have a MAD number  $\geq 1^\circ$ . Black lines indicate grain boundaries, defined by a  $10^\circ$  misorientation between adjacent points. Maps of the processed data, for which wild spikes have been removed and data extrapolated, are shown in (B) and (F). The map in (I) of the fine-grained area shows an alternative method of processing the data, in which the data is extrapolated prior to removing wild spikes. Pole figures of one orientation point per olivine grain are shown in (C), (D), (G), (H), and (J). All pole figures are equal area lower hemisphere projections, contoured using a  $15^\circ$  half width and as multiples of a uniform distribution (MUD) to a maximum of 3 MUD. Contouring of 1 MUD indicates no significant difference from a uniform distribution and corresponds to the absence of an LPO. The shear direction is parallel to the horizontal axis in the pole figures.

with zero, or null, solutions. In the processed data, pixels with zero solutions were replaced with the most common neighbor orientation. This method of processing the data minimizes the overcounting of individual grains when extracting one orientation point per grain for the construction of pole figures. However, it under-represents the smallest grains, which are close to the sampling step size and are filtered out with noise in the data.

Pole figures, shown in Figs. 2–4, were calculated using one point per grain, with all data sets containing  $\geq 180$  grains, which has been demonstrated to provide statistically robust results [15]. Grain boundaries were defined by misorientations  $\geq 10^\circ$  between adjacent points and subgrains by  $2^\circ$ – $10^\circ$  misorientations. Pole figures of raw and processed data in Fig. 2 demonstrate that in both the finer and coarser grained areas, the processing affects the strength of the lattice preferred orientation (LPO), but does not alter the overall LPO pattern. There are two main differences between the raw and processed data: (1) the removal of small grains, points with no solutions and wild spikes, which decreases the randomness of the data, leading to a stronger LPO and (2) extrapolation of the data, which further reduces the number of small grains but increases the randomness of the data, as groups of adjacent small grains with the same orientation are replaced by individual large grains.

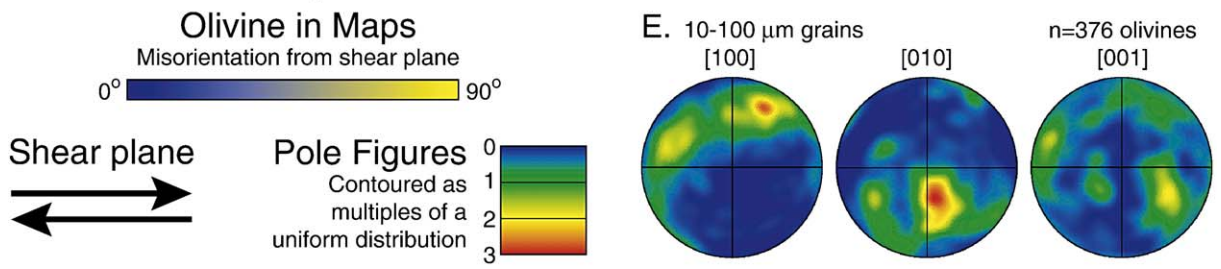
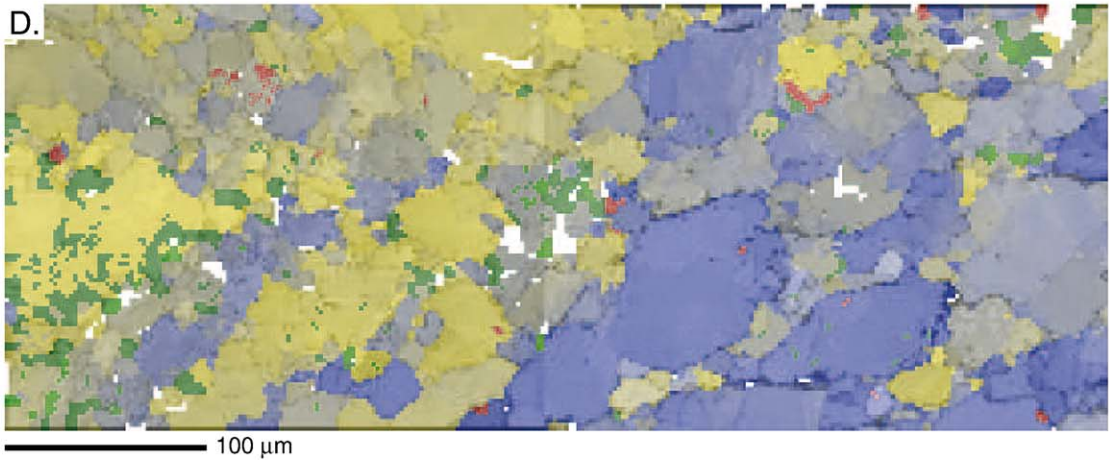
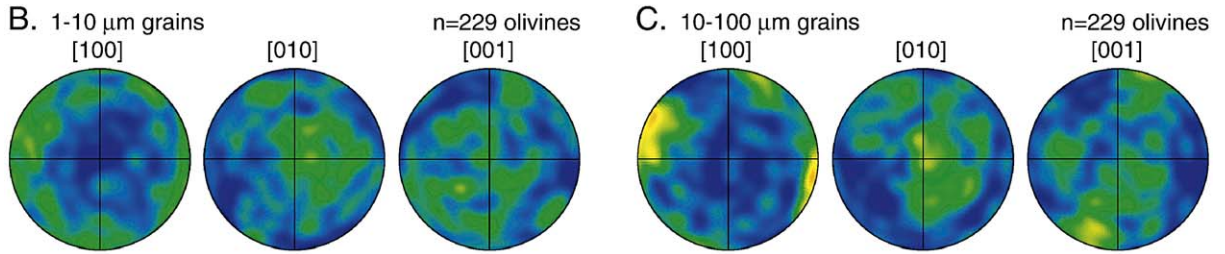
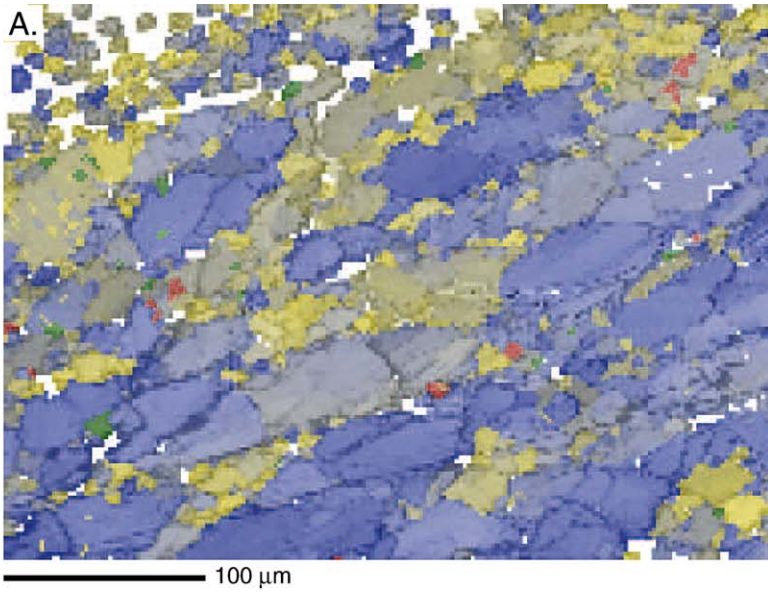
Using an alternative processing method, shown in Fig. 2I and J, data are extrapolated prior to the removal of wild spikes. This provides a better representation of the distribution of the pyroxene and spinel grains in the finest grained areas of the sample. However, as we wish to minimize potential bias in the olivine fabrics, we show data processed by the first method only in Figs. 3 and 4. These issues are inherent in analyzing such fine-grained material, which has a grain size close to the minimum step size.

### 3. Results

Microstructural observations of the mylonites indicate that grain size reduction leads to progressive localization of deformation into fine-grained bands. The influence of grain size on rheology can be seen in the optical-scale microstructures in Fig. 1. The mylonite consists of anastomosing bands of coarser ( $\leq 100 \mu\text{m}$ ) and finer ( $\leq 10 \mu\text{m}$ ) grained olivine, with distributed grains of orthopyroxene, clinopyroxene and spinel. Large, round to elongate porphyroclasts of olivine, orthopyroxene, clinopyroxene and spinel, ranging in size from 0.1 mm to 5 mm, are preserved in the fine-grained matrix. These microstructures indicate that the large porphyroclast grains behaved as hard inclusions during deformation. In some cases, these inclusions are

Fig. 3. Orientation maps collected by EBSD for two coarser grained areas of the mylonite (A, D). The area in (A) is also shown in Fig. 2; the area in (D) was collected at a 4  $\mu\text{m}$  step size, with 72% of the area indexed. Olivine is shaded from blue to yellow, with the color range representing the degree of misorientation of each pixel from the shear plane. Dark green corresponds to orthopyroxene, light green to clinopyroxene, red to spinel, and white areas have no data. Pole figures of one orientation per olivine for the area in (A) are shown for 1–10  $\mu\text{m}$  grains in (B) and for 10–100  $\mu\text{m}$  grains in (C). For the area in (D), data are only plotted for 10–100  $\mu\text{m}$  grains in (E), due to the large step size of the map. Contouring in all pole figures is to a maximum of 6 MUD. The shear direction is parallel to the horizontal axis in the pole figures.





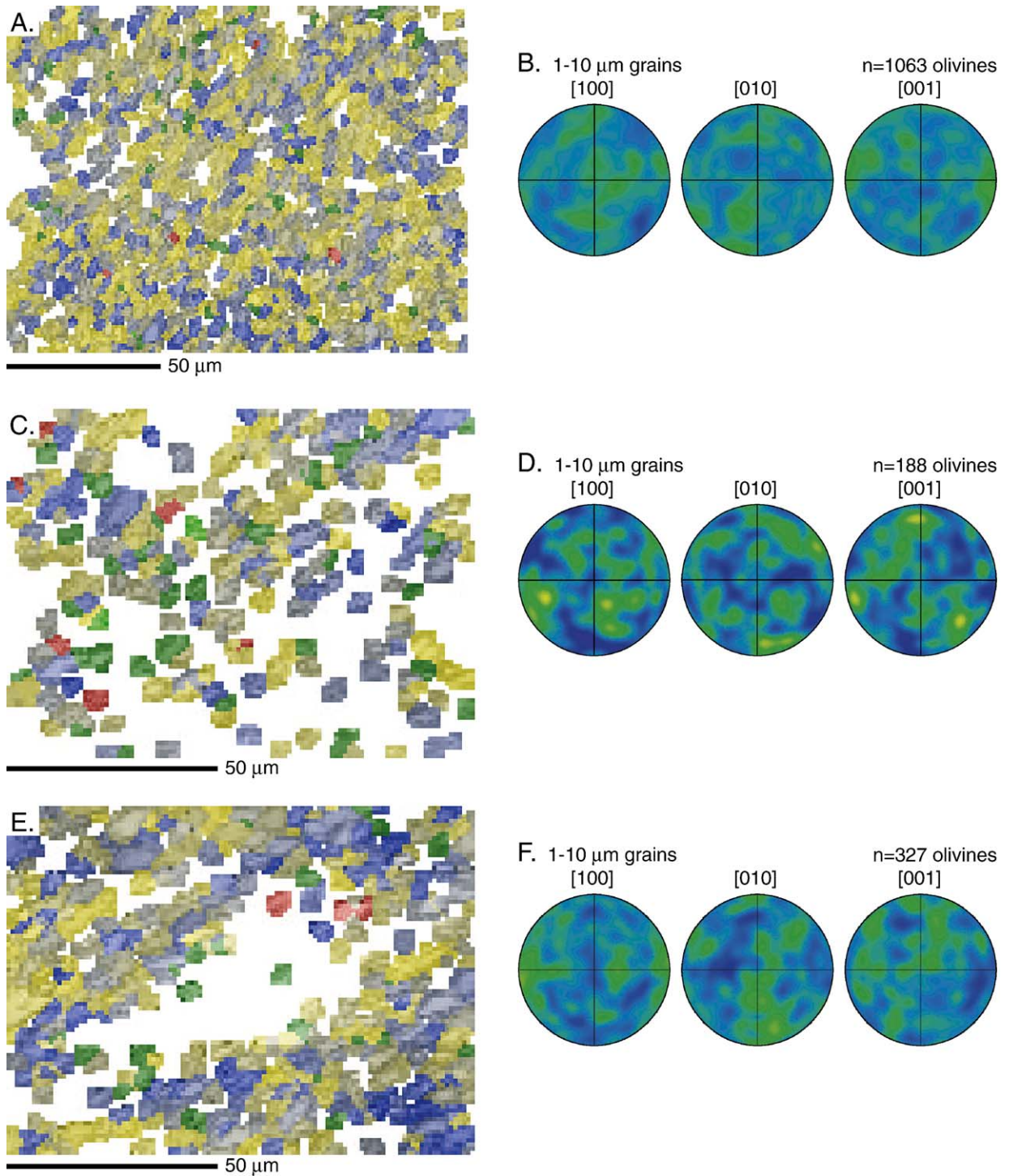


Fig. 4. Orientation maps for three finer grained areas of the mylonite (A, C, E), using the same color scheme as in Fig. 3. The area in (A) is also shown in Fig. 2; the area in (C) was collected at a 1  $\mu\text{m}$  step size, with 57% indexed; the area in (E) was also collected at a 1  $\mu\text{m}$  step size, with 58% of the area indexed. Pole figures of one orientation per olivine are shown (B, D, F) for the 3 areas, all of which have grain sizes of 1–10  $\mu\text{m}$ . The contour scale is the same as in Fig. 3, to a maximum level of 6 MUD. In the first area, the actual maximum is 2 MUD; in the second and third areas it is 3 MUD.



relatively coarse-grained aggregates of olivine (Fig. 1). Kinematic indicators, such as vergence of small folds and asymmetric recrystallization trails around porphyroclasts, indicate the relative sense of shear for the mylonite.

Olivine orientations in coarser and finer grained regions of the mylonite are shown in maps and pole figures in Figs. 3 and 4. The data are plotted with respect to the banding and lineation orientations, which we assume are equivalent to the shear plane for this high strain rock. Data are presented for two coarser grained regions of the mylonite in Fig. 3, with the pole figures divided into 1–10  $\mu\text{m}$  and 10–100  $\mu\text{m}$  size grains for each data set. In the first region (Fig. 3A–C), a [100] maximum is observed in the plane of the banding and subparallel to the lineation, while a [001] maximum is observed perpendicular to the banding. In some areas, the LPO is significantly stronger among 10–100  $\mu\text{m}$  grains than among 1–10  $\mu\text{m}$  grains. In the other coarse grained region, a pole figure is only shown for the 10–100  $\mu\text{m}$  size grains (Fig. 3E), due to the large step size at which this data set was collected. The [100] maximum is not oriented parallel to the banding. A variable LPO was also found by limited universal stage work on coarser grained regions in this sample [4].

In the finer grained regions, shown in Fig. 4, a decrease in LPO strength is observed in all three areas measured. Almost no LPO is observed in some regions of the fine-grained bands (Fig. 4A–F). Locally, in the fine-grained region shown in Fig. 4E and F, we find a weak and dispersed “ghost” of the LPO observed in the coarser-grained region in Fig. 3A–C.

The variation of LPO and grain size correlates with the secondary phase distribution. Pyroxenes and spinel are inhomogeneously distributed in the mylonite, with small grains of these phases predominant in regions with a smaller olivine grain size. Based on the very fine grain size, the raw data (Fig. 2A and E), and the alternative method of processing the data (Fig. 2I), the number of small orthopyroxene grains is greater than that shown in Figs. 3 and 4. The EBSD orientation maps highlight the larger number of secondary phases in finer grained areas relative to coarser grained areas (compare Fig. 2B to F). The finer grained areas have a smaller range of grain sizes and a more random distribution of secondary phases. In contrast, the coarser grained regions have a larger range of olivine grain sizes. Locally, small grains of secondary phases are mixed with small grains of olivine at the edges of larger olivine grains.

Fig. 2F and I provide lower and upper bounds on the amount of secondary phases pinning the grain boundaries in the finest grained areas. We have also examined back-scattered electron images and X-ray maps of

coarse- and fine-grained areas. These confirm our observation of a greater concentration of secondary phases in the finest grained areas. Similarly, high resolution EBSD and X-ray maps of Michibayashi and Mainprice [16,17] show a greater accumulation of secondary phases in finer grained regions of the peridotite mylonite in their study.

## 4. Discussion

### 4.1. Fabric variations with grain size

The variation in olivine fabric with grain size in the mylonite provides an opportunity to constrain grain size sensitive deformation mechanisms in the lithosphere. Three observations in particular can be exploited to constrain the deformation mechanisms: (i) randomization of a pre-existing LPO in the finest grained regions of the mylonite; (ii) observation of an LPO in coarser grained regions; (iii) the preservation of porphyroclasts.

The randomization of olivine LPO in the finest grained regions of the mylonite indicates a change in deformation mechanism to diffusion creep. Two observations suggest that the randomization of LPO occurred as deformation localized into fine-grained regions. First, a weak LPO is observed in one fine-grained area (Fig. 4F) which is similar to the LPO in a coarser grained area (Fig. 3B and C). Second, the LPO among 1–10  $\mu\text{m}$  grains in a coarser grained area is similar, but weaker, than that in the 10–100  $\mu\text{m}$  size fraction (Fig. 3B and C). We conclude that the randomization of LPO is related to grain rotations that occur during the grain boundary switching process, which is required during diffusion creep (e.g., [18]).

The LPO in the coarser grained regions indicates that a dislocation process accommodated deformation during the early stages of mylonitization. At the same time, the preservation of large, sometimes equant, porphyroclasts implies that the rheology is grain size sensitive. If the rheology was not grain size sensitive, then all grains should be deformed to the same degree and large, relatively undeformed porphyroclasts would not be preserved. Based on comparison to experimental studies, we suggest that deformation in the coarser grained bands occurred by dislocation accommodated grain boundary sliding (DisGBS). DisGBS is a grain size sensitive creep mechanism that was identified experimentally on the basis of rheologic data on olivine aggregates deformed near the transition between dislocation creep and diffusion creep [19,8]. Of particular significance for our analysis is that deformation by DisGBS has been shown to produce LPOs in calcite [20,21] and ice [22,23].

During DisGBS, strain is dominantly accommodated by the relative movement of grains (i.e. grain boundary sliding) and is limited by either this process or the movement of dislocations within grains on the easy slip system [24,8]. These two processes act in series, as deformation is not accommodated independently by either grain boundary sliding or easy slip. Thus the strain rate for DisGBS ( $\dot{\epsilon}_{\text{DisGBS}}$ ) is limited by the slowest of the two mechanisms through the relationship:

$$\dot{\epsilon}_{\text{DisGBS}} = \left( \frac{1}{\dot{\epsilon}_{\text{GBS}}} + \frac{1}{\dot{\epsilon}_{\text{Easy}}} \right)^{-1} \quad (1)$$

where  $\dot{\epsilon}_{\text{GBS}}$  is the strain rate for grain boundary sliding (GBS) and  $\dot{\epsilon}_{\text{Easy}}$  is the strain rate for easy slip. The grain size sensitivity of DisGBS results from the influence of grain size on the GBS component of the flow law.

There is considerable confusion regarding the terminology used for grain size dependent deformation mechanisms. For example, deformation in both the diffusion creep and DisGBS regimes involves grain boundary sliding, with relative grain movement accommodated either by diffusion or dislocation processes, respectively. Furthermore, the term superplasticity is often used when referring to deformation accommodated by GBS (see discussion in Goldsby and Kohlstedt [24]). To clarify our terminology, we refer to the serial deformation process (Eq. (1)) as DisGBS and the grain boundary sliding component of the process as GBS.

#### 4.2. Deformation mechanism maps

We use olivine deformation mechanism maps to constrain the deformation conditions of the mylonites (Fig. 5A). The total strain rate ( $\dot{\epsilon}_{\text{Total}}$ ) during deformation is contoured in stress versus grain size space, using the constitutive law [8]:

$$\dot{\epsilon}_{\text{Total}} = \dot{\epsilon}_{\text{Dif}} + \dot{\epsilon}_{\text{Dis}} + \dot{\epsilon}_{\text{LTP}} + \dot{\epsilon}_{\text{DisGBS}} \quad (2)$$

where  $\dot{\epsilon}_{\text{Dif}}$  is the strain rate for diffusion creep,  $\dot{\epsilon}_{\text{Dis}}$  for dislocation creep, and  $\dot{\epsilon}_{\text{LTP}}$  for low-temperature plasticity (LTP). The flow law formulation and experimental data for LTP are from [25,26]. These four deformation mechanisms are independent, so the mechanism with the fastest strain rate controls the rheology.

The boundaries for the fields of diffusion creep, dislocation creep, and DisGBS are calculated using a compilation of olivine experimental data from Hirth and Kohlstedt [8]. The flow laws for melt- and water-free aggregates in these regimes have the form:

$$\dot{\epsilon} = A \sigma^n d^{-m} \exp\left(-\frac{E + PV}{RT}\right) \quad (3)$$

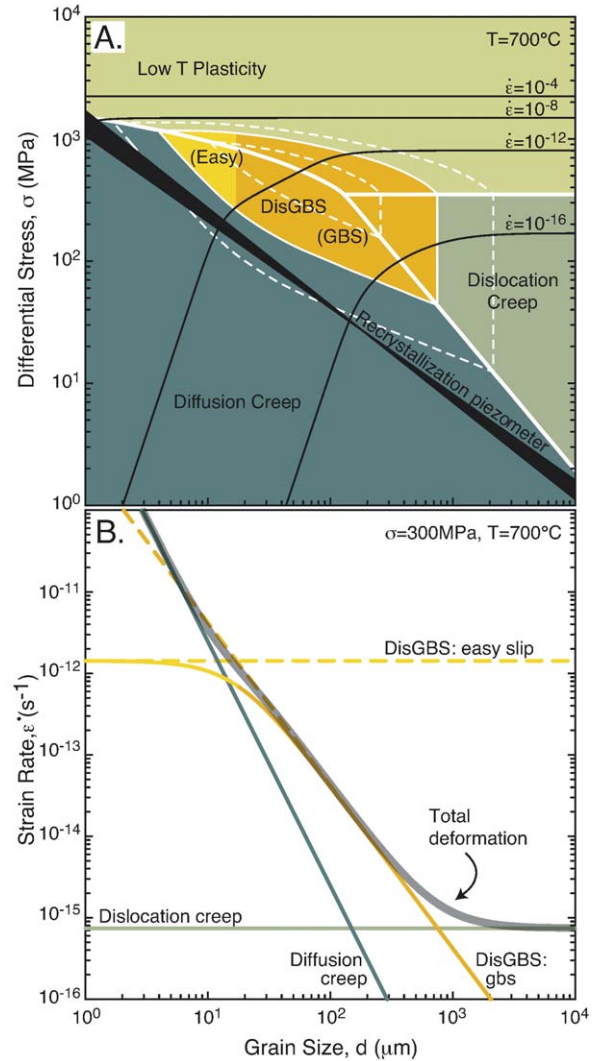


Fig. 5. (A) An olivine deformation mechanism map, on axes of differential stress versus grain size, contoured for strain rate, plotted using the flow laws for dry, melt free olivine at 700 °C and 12 km depth [25,26,8]. The black recrystallization piezometer field delimits the grain size predicted by the empirical piezometric relationship for olivine deformed under dry conditions [31,32]. The thick white boundaries between deformation fields indicate field boundaries in the absence of DisGBS. The thin white boundaries delineate the DisGBS field and the dashed boundaries on either side represent uncertainty in the location of the DisGBS boundaries due to uncertainty in its activation energy. The change in shading within the DisGBS field indicates the transition from the regime where creep on the easy slip system limits the strain rate to the regime where GBS limits the strain rate. (B) The variation of total and individual strain rates with grain size, at a differential stress of 300 MPa, and at 700 °C and 12 km depth. The dashed lines represent the individual components of DisGBS.

where  $A$  is a constant,  $\sigma$  is the differential stress,  $n$  is the stress exponent,  $d$  is the grain size,  $m$  is the grain size exponent,  $E$  is the activation energy,  $P$  is the pressure,  $V$



is the activation volume,  $R$  is the gas constant, and  $T$  is the absolute temperature. For the mylonite,  $d$  is in the range of 1–100  $\mu\text{m}$ . The deformation temperature is constrained from thermometry to lie in the range 600–750  $^{\circ}\text{C}$  [4]. We use a nominal pressure of 400 MPa for these calculations. The pressure of deformation is not well constrained, however the  $PV$  term in Eq. (3) is negligible for deformation in the shallow oceanic lithosphere.

Application of the experimental olivine data to the conditions of mylonite formation involves a significant extrapolation of temperature, but not of grain size or stress. Therefore, the greatest uncertainty in the map in Fig. 5A is in the activation energies for the deformation mechanisms. We calculated the error range for the field boundaries due to error in these activation energies. The activation energies for DisGBS are the most uncertain. For the grain boundary sliding component, the activation energy is assumed to be the same as that for the easy slip system, which is constrained experimentally at high temperature [27]. However, results from Carter and Ave'Lallemant [28] on the experimental deformation of dunites indicate that the easy slip system in olivine changes at low temperature. Despite uncertainty in the extrapolation to low temperature, the range of estimated mylonite deformation conditions lies within the DisGBS field, as shown in Fig. 5A.

To emphasize the conditions where DisGBS is a significant deformation mechanism, and its significance for LPO development, we plot strain rate versus grain size for a stress of 300 MPa in Fig. 5B. This plot represents a constant stress section through Fig. 5A. The total strain rate is dominated by DisGBS at grain sizes in the range  $\sim 15$ –700  $\mu\text{m}$ . Furthermore, the strain rate for DisGBS is at least an order of magnitude greater than that for dislocation creep at grain sizes  $< \sim 300$   $\mu\text{m}$ . The strain rate for diffusion creep becomes greater than that for DisGBS at grain sizes  $< \sim 15$   $\mu\text{m}$ . For comparison, at a grain size of  $\sim 15$   $\mu\text{m}$ , the strain rate for diffusion creep is approximately three orders of magnitude greater than that for dislocation creep. Assuming that LPOs form when a dislocation process accommodates a significant component of the total strain—and recalling that our microstructural observations indicate a randomization of LPO when grain size decreases below  $\sim 10$   $\mu\text{m}$ —we conclude that the LPOs observed in coarser grained regions of the mylonite resulted from DisGBS.

Our results suggest that an LPO is maintained during DisGBS when the easy slip component is dominant during deformation, though rate limited by the GBS component. Grain boundary sliding, whether diffusion or dislocation accommodated, tends to randomize LPOs. Prior and co-workers have demonstrated that a grain

boundary sliding process leads to an increased dispersion in the misorientation between grains, which weakens an initial single crystal LPO [7,29,30]. Our observation of a randomized LPO during diffusion creep supports the suggestion by Bestmann and Prior [29] that a grain boundary sliding process weakens LPOs.

#### 4.3. Recrystallization and grain boundary pinning

To understand how grain size sensitive creep promotes strain localization, we consider the processes that control the evolution of grain size during mylonite deformation. As deformation continues to lower temperature, and therefore higher stress, grain size decreases as a result of dynamic recrystallization. Empirical relationships between stress and grain size have been determined for olivine and this recrystallization piezometer [31,32] is shown in Fig. 5A. Dynamic recrystallization is driven by gradients in dislocation density, which promote subgrain rotation and grain boundary migration. In the diffusion creep field, the applicability of the empirical piezometer is problematic owing to a potential lack of driving force for recrystallization. This insight motivated the field boundary hypothesis [33,34], in which the piezometer is defined by the boundary between the dislocation creep and diffusion creep fields. Thus, the piezometric relationship may be temperature dependent due to differences in the activation energy for the creep processes. However, Drury [35] emphasized the lack of evidence for temperature dependence in the empirical relationships for olivine, based on the observation of statistically equivalent piezometric relationships for samples deformed at 1100–1300  $^{\circ}\text{C}$  [32] and at 1500  $^{\circ}\text{C}$  [31]. Thus, while the field boundary hypothesis has merit, the higher temperature experimental data indicate that a recrystallization piezometer applies within the dislocation creep regime.

The magnitude of grain size reduction in the mylonite can be explained by either the empirical piezometric relationship or a modified field boundary hypothesis. As illustrated in Fig. 5A, the grain size at which we see evidence for LPO randomization (i.e.,  $\sim 10$   $\mu\text{m}$ ) falls near the boundary between diffusion creep and DisGBS at geologic strain rates, consistent with a modified field boundary hypothesis in which the piezometer is defined by the diffusion creep/DisGBS field boundary, rather than the diffusion creep/dislocation creep field boundary. At the same time, the empirical piezometric relationship falls in the DisGBS field (within uncertainty), indicating that the driving force for recrystallization arises from the easy slip component of the DisGBS mechanism. In either case, we emphasize that the extreme grain size reduction

observed in the mylonites is difficult to explain without the DisGBS mechanism.

Grain boundary pinning can lead to permanent grain size reduction and a transition to diffusion creep. Without a mechanism to limit grain growth, grain size reduction may not promote a transition to diffusion creep in single phase materials, due to a dynamic balance between grain growth and recrystallization [33,34]. However, we suggest that the translation of grains during DisGBS by grain boundary sliding (and phase boundary sliding) results in the mixing of different mineral phases, which eventually inhibits grain growth. In the mylonite, the randomization of LPO in the fine-grained regions indicates that the presence of pyroxenes and spinel results in the pinning of olivine grain boundaries, leading to a transition to diffusion creep. Previous studies have emphasized the role of grain size pinning, resulting from fluid addition, melt crystallization or metamorphic reactions, in promoting grain size sensitive creep processes [9,11,6,10].

#### 4.4. Strain localization

To explore the implications of grain size sensitive creep mechanisms for strain localization in the oceanic lithosphere, in Fig. 6 we compare the viscosities of a fine-grained shear zone and the surrounding coarse-grained mantle. Based on our analysis of microstructural data and experimental flow laws, we assume that deformation in the shear zone occurs at a stress and grain size on the boundary between the DisGBS and diffusion creep fields on the deformation mechanism map, which leads to the relationships:

$$\dot{\epsilon}_{\text{DisGBS}} = \dot{\epsilon}_{\text{Dif}} \quad (4)$$

$$\dot{\epsilon}_{\text{SZ}} = \dot{\epsilon}_{\text{DisGBS}} + \dot{\epsilon}_{\text{Dif}} = 2 \dot{\epsilon}_{\text{DisGBS}} = 2 \dot{\epsilon}_{\text{Dif}} \quad (5)$$

where  $\dot{\epsilon}_{\text{SZ}}$  is the shear zone strain rate.

The effective viscosity ( $\eta$ ) of the shear zone in Fig. 6 is calculated using Eqs. (3) and (5), the relationship  $\eta = \sigma / \dot{\epsilon}_{\text{SZ}}$  and assuming  $\dot{\epsilon}_{\text{SZ}} = 10^{-12} \text{ s}^{-1}$ . The calculations are made for both the GBS and the easy slip components of DisGBS, as shown in Fig. 6. At temperatures greater than  $\sim 700 \text{ }^\circ\text{C}$ , viscosity in the shear zone is controlled by the GBS component of the DisGBS flow law and this component may dominate, within error, at lower temperatures as well.

The shear zone viscosity at  $700 \text{ }^\circ\text{C}$  is approximately four orders of magnitude lower than outside the shear zone (Fig. 6). Outside the shear zone, we assume (i) that dislocation creep accommodates deformation of the

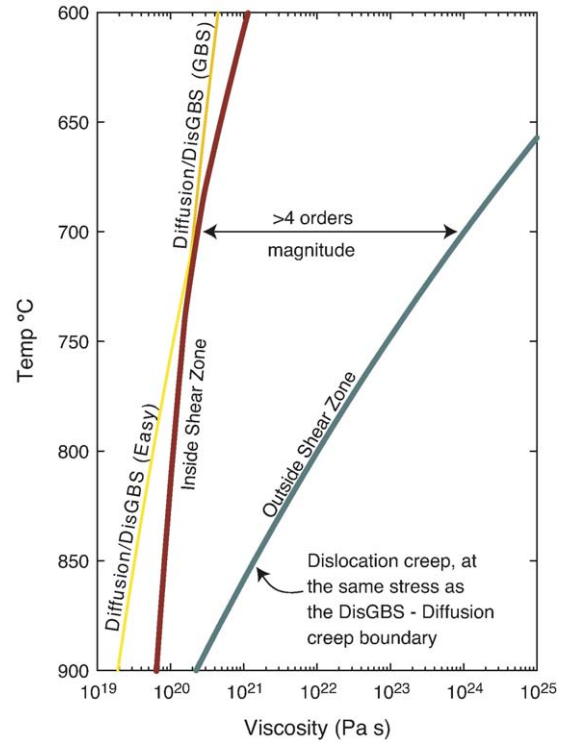


Fig. 6. The variation of effective viscosity with temperature, for deformation within a shear zone compared to that outside a shear zone. Within the shear zone, viscosity is defined by deformation at the DisGBS–diffusion creep boundary at a total strain rate of  $10^{-12} \text{ s}^{-1}$ . Deformation outside the shear zone is by dislocation creep, calculated at the same stress as within the shear zone.

coarse-grained mantle and (ii) that stress is limited by the strength of the shear zone. The effective viscosity for the shear zone remains lower than the coarse-grained mantle until a temperature of  $\sim 950 \text{ }^\circ\text{C}$ , at which point deformation is no longer localized. Where grain size pinning results in a transition to diffusion creep, the viscosity contrast would be even larger than that illustrated in Fig. 6. A convenient flow law for deformation in mantle shear zones – which accounts for grain size dependence – can be derived by solving Eq. (4) for grain size and substituting into Eq. (5):

$$\dot{\epsilon}_{\text{SZ}} = 2 \frac{A_{\text{DisGBS}}^3}{A_{\text{Dif}}^2} \sigma^{8.5} \exp\left(\frac{2H_{\text{Dif}} - 3H_{\text{DisGBS}}}{RT}\right) \quad (6)$$

where  $H = E + PV$ . Using the values for these parameters from [8], Eq. (6) can then be written as:

$$\dot{\epsilon}_{\text{SZ}} = 2.4 \times 10^{-7} \sigma^{8.5} \exp\left(\frac{-4.7 \times 10^5}{RT}\right) \quad (7)$$

for  $\sigma$  in MPa. This relationship is applicable for shear zone deformation at temperatures  $< 950 \text{ }^\circ\text{C}$  and



lithospheric depths, where the  $PV$  term is negligible. We reiterate that the largest uncertainty is related to the activation energy, as shown in Fig. 5A. At higher temperature, and therefore lower stress, errors associated with extrapolation in stress and grain size should also be considered.

#### 4.5. Relationship of mylonites to earthquake processes

A combination of geophysical, experimental and geochemical observations indicate that the transition from brittle to ductile processes occurs at a temperature of  $\sim 600$  °C in the oceanic lithosphere. Seismological studies of the depth of earthquakes along transform faults indicate that seismicity is confined to depths in the oceanic lithosphere with temperatures  $< 600$  °C (e.g., [36,37]). Extrapolation of experimental data for olivine aggregates indicates that the 600 °C isotherm also marks the transition from stable to unstable frictional sliding [38]. Finally, Jaroslow et al. [4] estimated that the minimum temperature for mylonite deformation is  $\sim 600$  °C, based on olivine–spinel geothermometry.

In Fig. 7, we compare the estimated strain rate for mylonite deformation to the strain rates for different geologic processes. The stress and strain rates of mylonite deformation are estimated using the microstructural observations combined with the olivine flow laws. From the recrystallization piezometer [31,32], the estimated differential stress for a recrystallized grain

size of 10  $\mu\text{m}$  is 240 MPa and of 3  $\mu\text{m}$  is 580 MPa. At 600–700 °C and these stress and grain size conditions, the estimated strain rate for mylonite deformation is  $10^{-14}$ – $10^{-10}$   $\text{s}^{-1}$ . The strain rate for post-seismic slip in Fig. 7 is calculated as:

$$\dot{\epsilon} = \left( \frac{\text{slip}}{\text{width}} \right) \times \left( \frac{1}{\Delta t} \right) \quad (8)$$

where  $\Delta t$  is the duration of post-seismic slip. The estimated strain rate for post-seismic slip is  $10^{-10}$ – $10^{-5}$   $\text{s}^{-1}$ , for slip  $< 1$  m, width  $\sim 1$  m to  $< 1$  km, and  $\Delta t \approx 1$ –100 days. Therefore, the estimated strain rate for mylonites overlaps the low end of post-seismic slip and the high end of tectonic strain rates (i.e.,  $10^{-15}$ – $10^{-12}$   $\text{s}^{-1}$ ). Our results place constraints on the conditions of deformation at the base of the seismogenic zone in the oceanic lithosphere, which may be used to interpret geodetic data for post-seismic slip (e.g., [39]).

#### 4.6. Mantle anisotropy

The microstructural observations of the mylonite demonstrate that the transition to diffusion creep results in a randomization of pre-existing LPOs. Evidence that pre-existing anisotropy may be destroyed by the transition to diffusion creep is important for understanding mantle anisotropy. In the upper mantle, seismic anisotropy reflects high temperature flow by dislocation creep [40–43]. However, with increasing depth and temperature in the mantle, the dominant mechanism of olivine deformation may change from dislocation creep to diffusion creep [44]. Our results indicate that such a change can lead to a decrease in mantle anisotropy, if enough strain is accumulated to randomize the fabric. We emphasize that in the case of shear zones, we do not expect fabric randomization to have a detectable effect on regional mantle anisotropy. However, following the suggestion of Karato and Wu [44] that a transition to diffusion creep may occur at depth in the upper mantle, our results imply that this would lead to an isotropic layer in the lower portion of the upper mantle.

## 5. Conclusions

Peridotite mylonites demonstrate that three orders of magnitude grain size reduction occurs during localized deformation in the oceanic lithosphere. Microstructural analyses of the mylonite fabric suggest that deformation of aggregates with a grain size of 10–100  $\mu\text{m}$  occurred by DisGBS and produces an LPO. Grain boundary

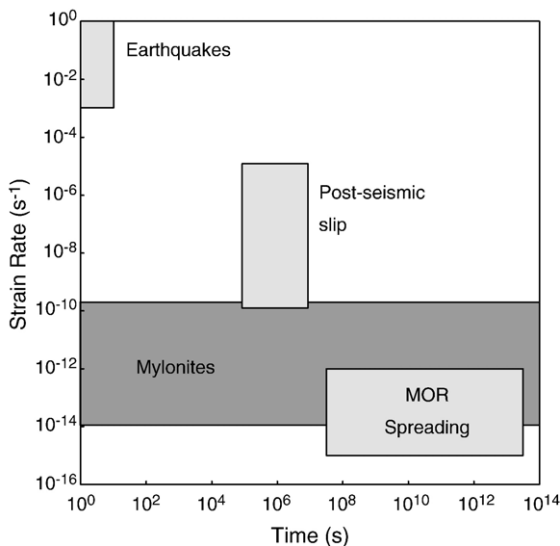


Fig. 7. Duration versus estimated strain rate for the mylonite and for earthquakes, post-seismic slip and plate spreading. Earthquakes last 1–10 s, post-seismic slip lasts 1–100 days, and spreading events from 1 yr to 1 My.

pinning, due to the mixing of pyroxenes and spinel among olivine grains during DisGBS, resulted in permanent grain size reduction. Reduction in grain size down to 1–10  $\mu\text{m}$ , combined with second phase pinning, led to a transition to diffusion creep and resulted in a randomization of the pre-existing LPO.

Our microstructural observations are consistent with extrapolation of experimental olivine flow laws to temperatures of 600–800  $^{\circ}\text{C}$  during mylonite deformation. The empirical recrystallization piezometer plots within the field of DisGBS, providing a driving force for grain size reduction. Alternatively, grain size reduction may have followed a modified version of the field boundary hypothesis [33,34]. At temperatures below  $\sim 950$   $^{\circ}\text{C}$ , deformation in the DisGBS and diffusion creep fields occurs at lower stress and viscosity than in the dislocation creep field, providing a mechanism for weakening and strain localization in the oceanic lithosphere at transform faults.

### Acknowledgements

We thank Henry Dick for bringing our attention to the peridotite mylonites. Louie Kerr provided invaluable assistance with the SEM at the Marine Biological Laboratory. In addition we would like to thank Margaret Boettcher, Mike Braun, Peter Kelemen, Jeff McGuire, and Laurent Montési for helpful discussions. Reviews by David Prior and an anonymous reviewer helped improve our manuscript. This work was supported by NSF Grant EAR-0230267 and a Hollister Fellowship from the WHOI Academic Programs Office.

### References

- [1] S.H. Kirby, Rock mechanics observations pertinent to the rheology of the continental lithosphere and the localization of strain along shear zones, *Tectonophysics* 119 (1985) 1–27.
- [2] J. Tullis, L. Dell'Angelo, R.A. Yund, Ductile shear zones from brittle precursors in feldspathic rocks: the role of dynamic recrystallization, in: A.G. Duba, W.B. Durham, J.W. Handin, H.F. Wang (Eds.), *The brittle–ductile transition in rocks*, Geophysical Monograph, vol. 53, American Geophysical Union, 1990, pp. 67–82.
- [3] M.R. Drury, R.L.M. Vissers, D. Van der Wal, E.H. Hoogerduijn Strating, Shear localisation in upper mantle peridotites, *Pure Appl. Geophys.* 137 (4) (1991) 439–460.
- [4] G.E. Jaroslow, G. Hirth, H.J.B. Dick, Abyssal peridotite mylonites: implications for grain-size sensitive flow and strain localization in the oceanic lithosphere, *Tectonophysics* 256 (1996) 17–37.
- [5] D. Jin, S.-I. Karato, M. Obata, Mechanisms of shear localization in the continental lithosphere: inference from the deformation microstructures of peridotites from the Ivrea zone, northwestern Italy, *J. Struct. Geol.* 20 (2/3) (1998) 195–209.
- [6] J. Newman, W.M. Lamb, M.R. Drury, R.L.M. Vissers, Deformation processes in a peridotite shear zone: reaction-softening by an  $\text{H}_2\text{O}$ -deficient, continuous net transfer reaction, *Tectonophysics* 303 (1999) 193–222.
- [7] Z. Jiang, D.J. Prior, J. Wheeler, Albite crystallographic preferred orientation and grain misorientation distribution in a low-grade mylonite: implications for granular flow, *J. Struct. Geol.* 22 (2000) 1663–1674.
- [8] G. Hirth, D. Kohlstedt, Rheology of the upper mantle and the mantle wedge: a view from the experimentalists, in: J. Eiler (Ed.), *The Subduction Factory*, Geophysical Monograph, vol. 138, American Geophysical Union, 2003, pp. 83–105.
- [9] R.L.M. Vissers, M.R. Drury, E.H. Hoogerduijn Strating, C.J. Spiers, D. van der Wal, Mantle shear zones and their effect on lithosphere strength during continental breakup, *Tectonophysics* 249 (1995) 155–171.
- [10] A.H. Dijkstra, M.R. Drury, R.L.M. Vissers, J. Newman, On the role of melt-rock reaction in mantle shear zone formation in the Othris peridotite massif (Greece), *J. Struct. Geol.* 24 (2002) 1431–1450.
- [11] M. Furusho, K. Kyuichi, Transformation-induced strain localization in a lherzolite mylonite from the Hidaka metamorphic belt of central Hokkaido, Japan, *Tectonophysics* 313 (1999) 411–432.
- [12] G. Hirth, D.L. Kohlstedt, Water in the oceanic upper mantle: implications for rheology, melt extraction and the evolution of the lithosphere, *Earth Planet. Sci. Lett.* 144 (1996) 93–108.
- [13] K.T.M. Johnson, H.J.B. Dick, N. Shimizu, Melting in the oceanic upper mantle: an ion microprobe study of diopsides in abyssal peridotites, *J. Geophys. Res.* 95 (1990) 2661–2678.
- [14] J.M. Warren, N. Shimizu, H.J.B. Dick, Melt impregnation revealed by clinopyroxene geochemistry in abyssal peridotites, *Geochim. Cosmochim. Acta* 67 (2003) A526.
- [15] W. Ben Ismail, D. Mainprice, An olivine fabric database: an overview of upper mantle fabrics and seismic anisotropy, *Tectonophysics* 296 (1998) 145–157.
- [16] K. Michibayashi, D. Mainprice, Understanding the deformation of rocks from the earth's mantle using simultaneous EBSD and EDS, [www.hkltechnology.com/data/0-mantle.pdf](http://www.hkltechnology.com/data/0-mantle.pdf), 2003.
- [17] K. Michibayashi, D. Mainprice, The role of pre-existing mechanical anisotropy on shear zone development within oceanic mantle lithosphere: an example from the Oman ophiolite, *J. Petrol.* 45 (2) (2004) 405–414.
- [18] R. Raj, M.F. Ashby, On grain boundary sliding and diffusional creep, *Metall. Trans.* 2 (1971) 1113–1127.
- [19] G. Hirth, D.L. Kohlstedt, Experimental constraints on the dynamics of the partially molten upper mantle: 2. Deformation in the dislocation creep regime, *J. Geophys. Res.* 100 (1995) 15441–15449.
- [20] S.M. Schmid, R. Panozzo, S. Bauer, Simple shear experiments on calcite rocks: rheology and microfabric, *J. Struct. Geol.* 9 (5/6) (1987) 747–778.
- [21] E.H. Rutter, M. Casey, L. Burlini, Preferred crystallographic orientation development during the plastic and superplastic flow of calcite rocks, *J. Struct. Geol.* 16 (10) (1994) 1431–1446.
- [22] W.B. Durham, L.A. Stern, S.H. Kirby, Rheology of ice I at low stress and elevated confining pressure, *J. Geophys. Res.* 106 (6) (2001) 11031–11042.
- [23] D.L. Goldsby, D.L. Kohlstedt, Reply to comment by P. Duval and M. Montagnat on “Superplastic deformation of ice: experimental observations”, *J. Geophys. Res.* 107 (B11) (2002) 2313.
- [24] D.L. Goldsby, D.L. Kohlstedt, Superplastic deformation of ice: experimental observations, *J. Geophys. Res.* 106 (B6) (2001) 11017–11030.



- [25] C. Goetze, The mechanisms of creep in olivine, *Philos. Trans. R. Soc. Lond.*, A 288 (1978) 99–119.
- [26] B. Evans, C. Goetze, The temperature variation of hardness of olivine and its implication for polycrystalline yield stress, *J. Geophys. Res.* 84 (1979) 5505–5524.
- [27] Q. Bai, S.J. Mackwell, D.L. Kohlstedt, High-temperature creep of olivine single crystals: 1. Mechanical results for buffered samples, *J. Geophys. Res.* 96 (B2) (1991) 2411–2463.
- [28] N.L. Carter, H.G. Ave'Lallemant, High temperature flow of dunite and peridotite, *Geol. Soc. Amer. Bull.* 81 (1970) 2181–2202.
- [29] M. Bestmann, D.J. Prior, Intragranular dynamic recrystallization in naturally deformed calcite marble: diffusion accommodated grain boundary sliding as a result of subgrain rotation recrystallization, *J. Struct. Geol.* 25 (2003) 1597–1613.
- [30] C.D. Storey, D.J. Prior, Plastic deformation and recrystallization of garnet: a mechanism to facilitate diffusion creep, *J. Petrol.* 46 (12) (2005) 2593–2613.
- [31] S.-I. Karato, M. Toriumi, T. Fujii, Dynamic recrystallization of olivine single crystals during high-temperature creep, *Geophys. Res. Lett.* 7 (9) (1980) 649–652.
- [32] D. Van der Wal, P. Chopra, M. Drury, J. Fitz Gerald, Relationships between dynamically recrystallized grain size and deformation conditions in experimentally deformed olivine rocks, *Geophys. Res. Lett.* 20 (14) (1993) 1479–1482.
- [33] J.H.P. De Bresser, C.J. Peach, J.P.J. Reijs, C.J. Spiers, On dynamic recrystallization during solid state flow: effects of stress and temperature, *Geophys. Res. Lett.* 25 (18) (1998) 3457–3460.
- [34] J.H.P. De Bresser, J.H. Ter Heege, C.J. Spiers, Grain size reduction by dynamic recrystallization: can it result in major rheological weakening? *Int. J. Earth Sci.* 90 (2001) 28–45.
- [35] M.R. Drury, Dynamic recrystallization and strain softening of olivine aggregates in the laboratory and the lithosphere, in: D. Gapais, J.P. Brun, P.R. Cobbold (Eds.), *Deformation Mechanisms, Rheology and Tectonics: From Minerals to the Lithosphere*, Special Publication of the Geological Society of London, vol. 243, Geological Society of London, 2005, pp. 143–158.
- [36] J.F. Engeln, D.A. Wiens, S. Stein, Mechanisms and depths of Atlantic transform earthquakes, *J. Geophys. Res.* 91 (B1) (1986) 548–577.
- [37] R.E. Abercrombie, G. Ekström, Earthquake slip on oceanic transform faults, *Nature* 410 (2001) 74–77.
- [38] M.S. Boettcher, G. Hirth, B. Evans, Olivine friction at the base of oceanic seismogenic zones, *J. Geophys. Res.* (in press).
- [39] L.G.J. Montési, G. Hirth, Grain size evolution and the rheology of ductile shear zones: from laboratory experiments to post-seismic creep, *Earth Planet. Sci. Lett.* 211 (2003) 97–110.
- [40] A. Nicolas, N.I. Christensen, Formation of anisotropy in upper mantle peridotites—a review, in: K. Fuchs, C. Froidevaux (Eds.), *Composition, Structure and Dynamics of the Lithosphere–Asthenosphere System*, Geodynamics Series, vol. 16, American Geophysical Union, 1987, pp. 111–123.
- [41] C.E. Nishimura, D.W. Forsyth, The anisotropic structure of the upper mantle in the Pacific, *Geophys. J.* 96 (1989) 203–229.
- [42] D. Mainprice, P.G. Silver, Interpretation of SKS-waves using samples from the subcontinental lithosphere, *Phys. Earth Planet. Inter.* 78 (1993) 257–280.
- [43] H. Jung, S.-I. Karato, Water-induced fabric transitions in olivine, *Science* 293 (2001) 1460–1463.
- [44] S.-I. Karato, P. Wu, Rheology of the upper mantle: a synthesis, *Science* 260 (1993) 771–778.